Acta Metallurgica Sinica (English Letters) (2024) 37:17–28
https://doi.org/10.1007/s40195-023-01654-0

Laser Powder Bed Fusion of Beta-Type Titanium Alloys for Biomedical Application: A Review

Xuan Luo[1] · Chao Yang[2] · Dongdong Li[1] · Lai-Chang Zhang[3]

Received: 4 October 2023 / Revised: 5 December 2023 / Accepted: 7 December 2023 / Published online: 28 January 2024

Abstract
Additive manufacturing of β-type titanium alloy is expected to replace Ti–6Al–4V alloy in the field of orthopedic implantation because of their low elastic modulus, excellent corrosion resistance, and biocompatibility. After briefly introducing the laser powder bed fusion (LPBF) process and physical phenomena, this paper reviews the recent progresses in LPBF-ed β-type Ti alloys. The strategies to strengthening and toughening β-type Ti alloys are critically reviewed. This is followed by the processing routes employed to achieve to low modulus for orthopedic applications, especially a new methodology for tailoring crystallographic orientation called multi-track coupled directional solidification. The effect of processing and compositions on performance metrics of β-type Ti alloys included corrosion behavior, and biocompatibility is reviewed. In the end, challenges in additive manufacturing of β-type Ti alloys in future are highlighted, with the aim to ensue clinical application of LPBF-ed β-type Ti alloys.

Keywords β-type Ti alloys · Laser powder bed fusion · Mechanical properties · Elastic modulus · Biocompatibility

1 Introduction

Currently, orthopedic implants have been rapidly developed with the advancement of human aging process and the strong demand for health consumption upgrading [1]. According to the Organisation for Economic Co-operation and Development (OECD), the utilization of hip implants continues to increase at a compound annual growth rate of 1.2% and is expected to increase to 2.8 (2.6–2.9) million by the year 2050 (from 1.8 million per year in 2015) [2]. Ti–6Al–4V alloy has become one of most ideal implant materials due to their good biocompatibility and mechanical properties, and are widely used in orthopedic screws, hip replacement implants, spinal fusion cages, dental implants, and other fields [3, 4]. However, Al may increase the risk of breast cancer and other neurological conditions, such as Alzheimer's disease. V and its compounds may result in carcinogenicity and various adverse effects on the respiratory system, blood parameters, liver, neurological system, and other organs [3, 5]. Besides, its elastic modulus is much higher (110 GPa) than that of human bone (10–30 GPa) [3]. The elastic mismatch between the bone and implant reduces the load experienced by the bone, triggers stress shielding effects, finally causes reduction in bone density around the implant, and leads to loosening of the implant [6]. β-type Ti alloys have evolved to become most potential orthopedic implant materials due to low elastic modulus (40–80 GPa) and non-toxic [7–9]. At present, the most widely studied β-type Ti alloys are included Ti–Nb-based, Ti–Mo-based, and Ti–Ta-based alloys, such as Ti–45Nb [10], Ti–13Nb–13Zr [11], Ti–35Nb–7Zr–5Ta

Available online at http://link.springer.com/journal/40195

✉ Chao Yang
cyang@scut.edu.cn

✉ Dongdong Li
lidongdong0@hust.edu.cn

✉ Lai-Chang Zhang
l.zhang@ecu.edu.au

[1] State Key Laboratory of Materials Processing and Die & Mould Technology, Huazhong University of Science and Technology, Wuhan 430074, China

[2] National Engineering Research Center of Near-Net-Shape Forming for Metallic Materials, Guangdong Provincial Key Laboratory for Processing and Forming of Advanced Metallic Materials, South China University of Technology, Guangzhou 510640, China

[3] Centre for Advanced Materials and Manufacturing, School of Engineering, Edith Cowan University, 270 Joondalup Drive, Joondalup, Perth, WA 6027, Australia

[12], Ti–35Nb–2Ta–3Zr [13], Ti–24Nb–4Zr–8Sn [14, 15], Ti–15Mo [16], and Ti–25Ta [17]. The development of β-type Ti alloys is focused on three considerations as follows: design of alloy composition, thermo-mechanical processing, and performance evaluation. The approaches of alloy compositions design are mainly involved as molybdenum equivalent (Mo_{eq}) [1], d-electron method [18], and valence electron concentration [19]. Besides, β-type Ti alloys are thermo-mechanically processed to increase their strength while maintaining low modulus. However, the mechanical properties and elastic modulus of β-type Ti alloys prepared by traditional processing methods are difficult to achieve great breakthroughs to meet patients' pursuit of higher quality and healthy life.

Additive manufacturing (AM), as an intelligent manufacturing technology, allows parts to be designed and machined without being constrained by geometry [20–25]. Therefore, AM processes have pioneered optimum success in bone tissue engineering such as enabling new model approaches and capability of precisely reproducing patient-specific implants. In other words, acceleration of healing and customized mechanical properties can be achieved through AM [9, 26]. Especially, combined with the processing characteristics of AM, the prepared Ti alloys often have better mechanical properties than the traditional process [27–29]. Among different AM technologies, laser powder bed fusion (LPBF) is the most widely used process for producing Ti implants due to the ability to enhance mechanical properties and feature complexity [26]. Up to now, most of the research focuses on the influence of LPBF process parameters on forming quality (involving the formation of pores and cracks) [30–32], microstructure and mechanical properties [33, 34]. It is gratifying that researchers have made surprising achievements in the acknowledgement of processing principle of LPBF and the tailoring of microstructure and desired mechanical properties [35–38]. However, a detailed topical review on LPBF-ed β-type Ti alloys for orthopedic applications is not available despite the rapid advances in this field and serves as the theme of this article. Specifically, strengthening and toughening, strategies to Young's modulus reduction, corrosion resistance, and biocompatibility of LPBF-ed β-type Ti alloys are systematically reviewed here.

2 Laser Powder Bed Fusion (LPBF)

Laser powder bed fusion (LPBF) is a micro-area rapid solidification process, which adopts layer-by-laser melting of the powder, using a high-energy laser beam(s) in an inert atmosphere, the melting sequence being in accordance with the CAD [8, 39–41]. The whole process involves fusing the initial powder layer onto the base substrate, initially leveling it on the build platform, and then stacking subsequent powder layers on top of the curing layer in turn until the final part is complete [42, 43]. Part optimization in LPBF typically requires control of key process parameters, including laser power, scanning speed, hatch spacing, and layer thickness which decides energy density, E (J/mm^3). Due to the different thermal histories of the materials and the different irradiation sources used to produce the parts, the energy density used for different materials and machines can also vary greatly. Therefore, it is generally necessary to explore the process parameters of alloys to determine the optimal process parameter window at initial LPBF process, especially for new materials.

Material solidification in the LPBF process differs from traditional cast, where the melt solidification depends largely on rapid temperature changes, gravity effects, and melt convection without the application of external pressure. In the LPBF process, the laser power, scanning speed, scanning spacing, powder thickness, preheating temperature, and other process parameters will affect the melt pool size, temperature gradient, and cooling rate [44]. Meanwhile, various physical phenomena and metallurgical reactions inside the melt pool are closely related to these process parameters [45]. When the powder bed is irradiated by the laser, the laser reflects on the surface of the powder for many times, making the laser penetrate continuously along the depth direction. The powder absorbs the photon energy and converts it into heat energy. The absorbed heat energy distribution depends on the apparent density and reflectivity of the powder in the top powder layer. The powder instantly reaches the melting point to form a melt pool, at which time a variety of physical phenomena will occur in and around the melt pool [45]. First of all, the powder melts to form a melt pool of several hundred microns or even millimeters, and the molten metal liquid inside the melt pool is convective under external forces such as viscosity, gravity, surface tension, capillary action, Marangoni convection, and evaporation pressure [46, 47]. Depending on the process and material, these forces can have different effects. The melt pool life is usually short, the viscosity is very low, and the effect of gravity is small compared to the effect of other forces [48]. The unstable melt pool will split under the action of Rayleigh–Taylor instability and form a single molten sphere under surface tension, that is, balling occurs [49–52]. The Marangoni force induces fluid movement away from the peak temperature of the melt pool center and accelerates heat transfer [53, 54]. Due to the high temperature of the melt pool, the material is easy to evaporate, and the resulting recoil pressure drives the fluid movement, while these pressures lead to the formation of so-called keyholes [30]. In addition, the recoil pressure also drives the powder near the molten pool, producing what is known as splashing and denudation [55]. Besides, selective evaporation of volatile elements changes the local and global material composition

[56]. After the material melts and consolidates, the temperature decreases and the material solidifies. Material shrinkage during solidification will cause stress in the surrounding material, which can be partially relaxed during the subsequent process [57]. It should be noted that the residual stress inside the component is the main cause of deformation [47, 58]. The above physical processes and metallurgical phenomena are completed in an instant, resulting in an extremely fast cooling rate (10^3–10^8 K/s) inside the melt pool. It can be seen that LPBF can be regarded as the rapid solidification of a small region. Complex physical phenomena and metallurgical processes occur in and around the melt pool, which will directly affect the microstructure and mechanical properties of the alloy. Therefore, these phenomena have to be considered in the alloy design and microstructure property regulation. Figure 1 shows the dynamic physical phenomena inside the molten pool during melting [45].

3 Strengthening and Toughening of LPBF Biomedical β-Type Titanium Alloy

The yield strength of alloys is closely related to their composition and microstructure. Traditional manufacturing routes such as forging, rolling, and heat treatment improve the strength through grain boundary strengthening, dislocation strengthening, and precipitation strengthening. Similarly, due to the characteristics of LPBF technology such as fast cooling rate, high thermal stress, and in situ cyclic heat treatment, the prepared alloys generally have smaller grain size, micro-/nanoparticle precipitation phase, and higher dislocation density, thereby high strength [27, 29, 59]. By optimizing process parameters, the distinct microstructures and improved strength can be achieved. For example, the LPBF-ed Ti–15Mo alloy using different energy densities has a strength improvement of nearly 200 MPa compared to traditional processing techniques such as rolling and forging [16]. This is due to the rapid temperature rise and drop during the LPBF process, which results in the alloy having smaller grain size and higher dislocation density. Likewise, Prashanth et al. utilized the rapid solidification of microregion to introduce high-density geometrically necessary dislocations in Ti–35Nb–7Zr–5Ta alloy, which increased its strength by approximately 137 MPa compared to spark plasma sintering [60]. In addition to utilizing the rapid cooling, the in situ cyclic heat treatment during LPBF is easy to induce precipitates in β-type titanium alloys, eventually result in the high strength. For example, Fig. 2 illustrates the morphology and distribution of secondary phases of LPBF-ed Ti–12Mo–6Zr–2Fe alloy using transmission electron microscopy (TEM) [61]. The HAADF-STEM image (Fig. 2c-d) further reveals the distribution of α″ phase, with three variants, inside the matrix grains. EDX elemental maps (Fig. 2e–f) of a representative area containing α″ phase triangle show that there is a pronounced composition difference between α″ and the β phase matrix. The high-density α″ phase could cause a strength of up to 1291 MPa but almost no plasticity. It is interesting that the use of checkerboard scanning strategy can change the peak temperature, cooling rate and temperature oscillation area, so as to avoid the brittle ω phase precipitation and achieve high strength and high plasticity ($\sigma_s = 1026$ MPa, $\varepsilon_f = 12.7\%$, Fig. 2i). Unlike in situ heat treatment with LPBF, the precipitation can also be achieved through post-treatment to achieve strengthening

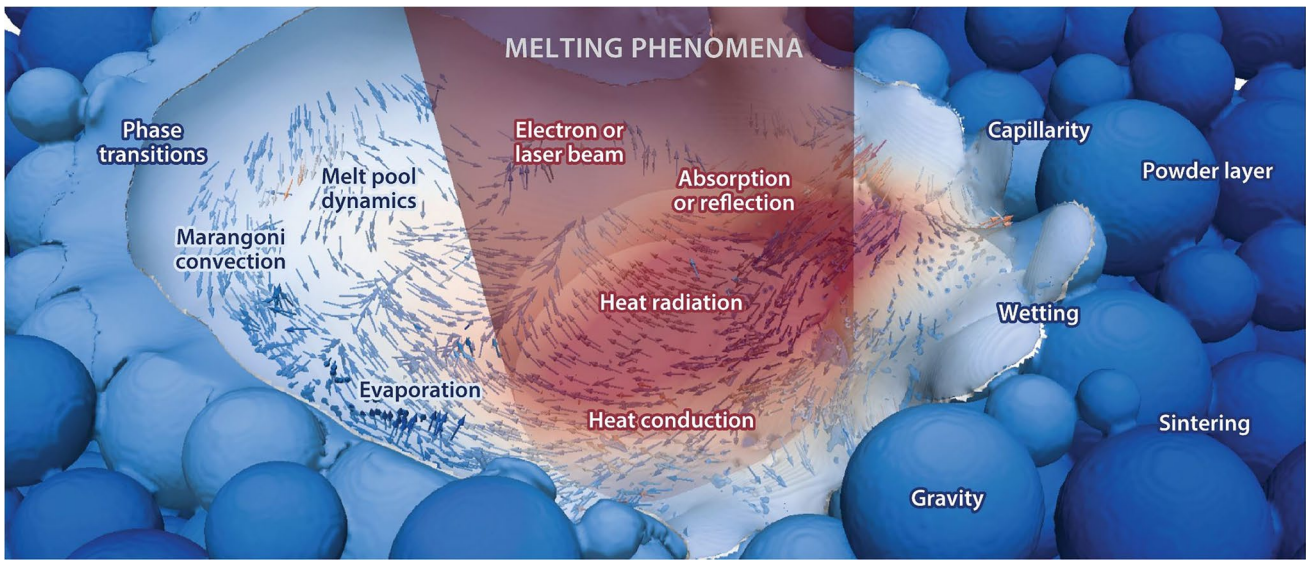

Fig. 1 Dominant physical phenomena during melting [45]

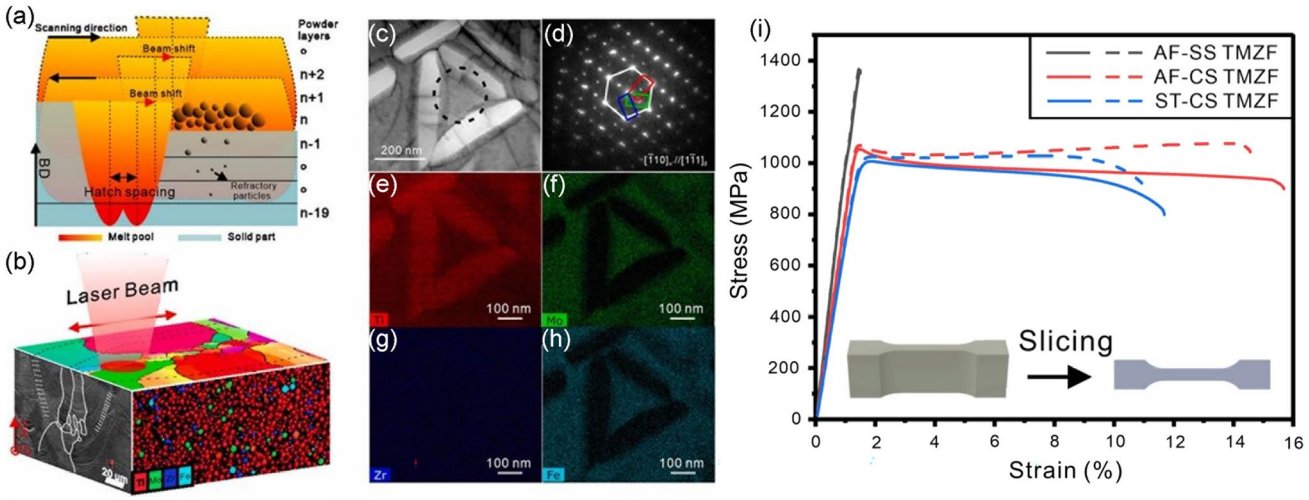

Fig. 2 **a** A schematic represents in situ heat treatment during the laser remelts; **b** a 3D morphology of LPBF-ed Ti–12Mo–6Zr–2Fe sample; **c** bright-field TEM image of a selected area containing α″ phase; **d** the SAED pattern along the $[\bar{1}11]_{\beta}$ zone axis collected from the black dotted circle in **c** showing the orientation relationship of $[\bar{1}10]_{\alpha''}//[\bar{1}11]_{\beta}$; **e**–**h** EDX elemental maps of Ti, Mo, Zr, and Fe collected from **c**, respectively; **i** the engineering (solid lines) and true (dotted lines) stress–strain curves of as-fabricated simple-scanned (AF-SS), (chess-scanned) AF-CS, and (solution heat-treated chess-scanned) ST–CS Ti–12Mo–6Zr–2Fe alloys [61]

in Ti–13Nb–13Zr alloy [62] or obtain superior functional properties in NiTi alloys [34]. For example, a stable and high tensile recovery strain was obtained in the heat-treated NiTi alloys owing to the formation of the Ni4Ti3 nanoprecipitate, which can induce the saturation of the dislocations formed at critical tensile cycles. Besides, combining with the differences in nucleation and grain growth in different regions of the melt pool can also obtain good mechanical properties. Typical heterogeneous structure consisting of a bimodal structure with fine grains wrapped in coarse grains can achieve a good combination of strength and plasticity because of the back stress [59, 63].

Not limited to grain boundary strengthening, dislocation strengthening, precipitation strengthening, if combined with LPBF forming principle, alloy system, and other unique characteristics, it is possible to obtain unexpected results. Generally, the deformation mode of the metastable β-type Ti alloys gradually changes from strain-induced α″ martensitic transformation, strain-induced ω phase transformation, {332}⟨113⟩ twining, {112}⟨111⟩ twining, and dislocation slip with the increase of β phase stability, and the corresponding yield strength gradually increases [64]. By means of traditional plastic deformation, high-density dislocations, twinning, and martensite can be introduced to improve the yield strength, but inevitably reducing plasticity. LPBF has the characteristics of rapid solidification, and high thermal stress is easy to induce twin, martensite, and high-density dislocation in metastable β-type Ti alloys such as Ti–35Nb–7Zr–Ta alloy. The superfine {112}⟨111⟩ twin with coherent ω phase interface can continuously prevent dislocation slip, and realize strain delocalization by assisting twin growth to release the stress concentration caused by dislocation plug at the front of phase interface, and finally obtain excellent mechanical properties (Fig. 3). This strategy improving the mechanical properties of β-type Ti alloys by introducing crystalline defects (dislocations, twins, etc.) was defined as defect engineering in Ref. [28]. In order to obtain better mechanical properties, a new idea of tailoring mechanical properties of Ti–35Nb–7Zr–Ta alloy based on metastable phase interception is proposed in Fig. 4. Figure 4a shows that a schematic diagram (Fig. 4a) of the microstructure evolution and corresponding globularization mechanism with different heat treatment times. In the I stage, the continuous thin shell-shaped S1 phase to split into segments and getting discontinuous by termination migration. In the II stage, the S1 phase gradually dissolved and the Si atoms diffused form the S1 phases into β-Ti matrix, resulting in the transition of S1 → $(Ti, Nb, Zr)_2Si$ (S2) phases. In the last III stage, coarsening or dissolution of S2 phase with different sizes is mainly controlled by Ostwald ripening, causing a decrease in the number of the S2 phase at the grain boundaries. Figure 4b, c shows the evolution of silicide after heat treatment. Ultimately, exhibiting ultra-high yield strength of 978 MPa and large elongation of 10.4%, occupying an outstanding regime in the strength and ductility space of Ti–Nb–Zr–Ta alloys in Fig. 4d. Simply put, non-equilibrium rapid solidification of LPBF trapped the continuously distributed ultra-fine S1 metastable phase at the grain boundaries and poor plasticity. After heat treatment, the "termination migration" promoted the continuous S1 phase transform into intermittent spherical particles and transforming S1 metastable phase into intermittent S2

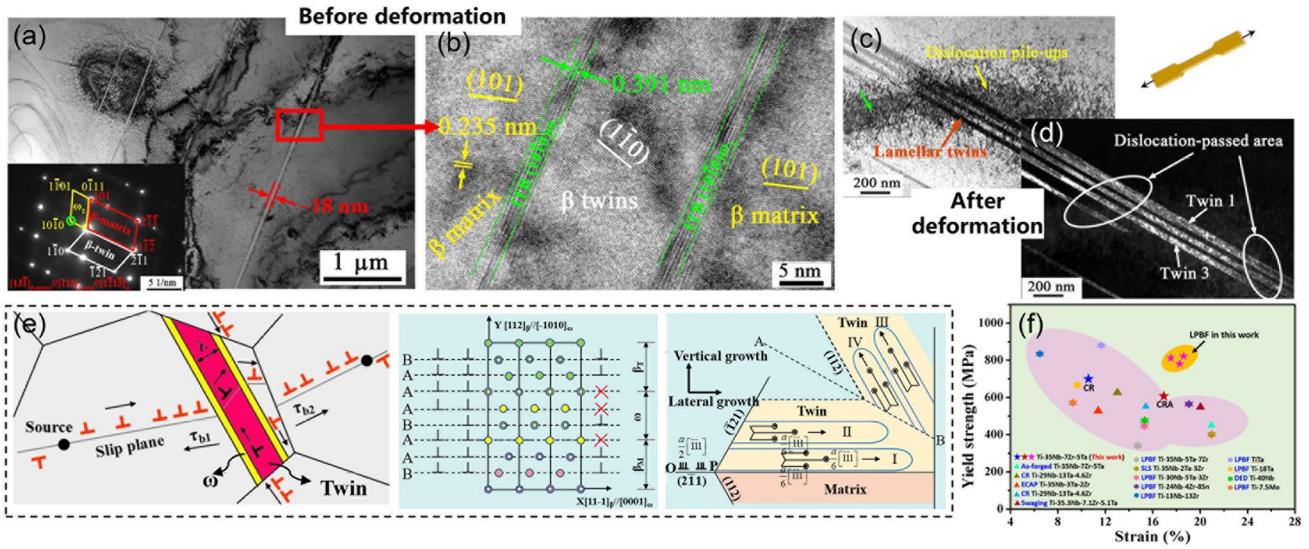

Fig. 3 Lamellar mechanical twins in LPBF-ed Ti–35Nb–7Zr–5Ta alloy before **a**, **b** and after **c**, **d** deformation, **e** schematic illustration of interaction mechanism between twin and dislocation during tensile deformation, **f** tensile yield strength vs elongation of the Ti–35Nb–7Zr–5Ta alloy samples and other representative β-Ti alloys fabricated by various materials processing methods [28]

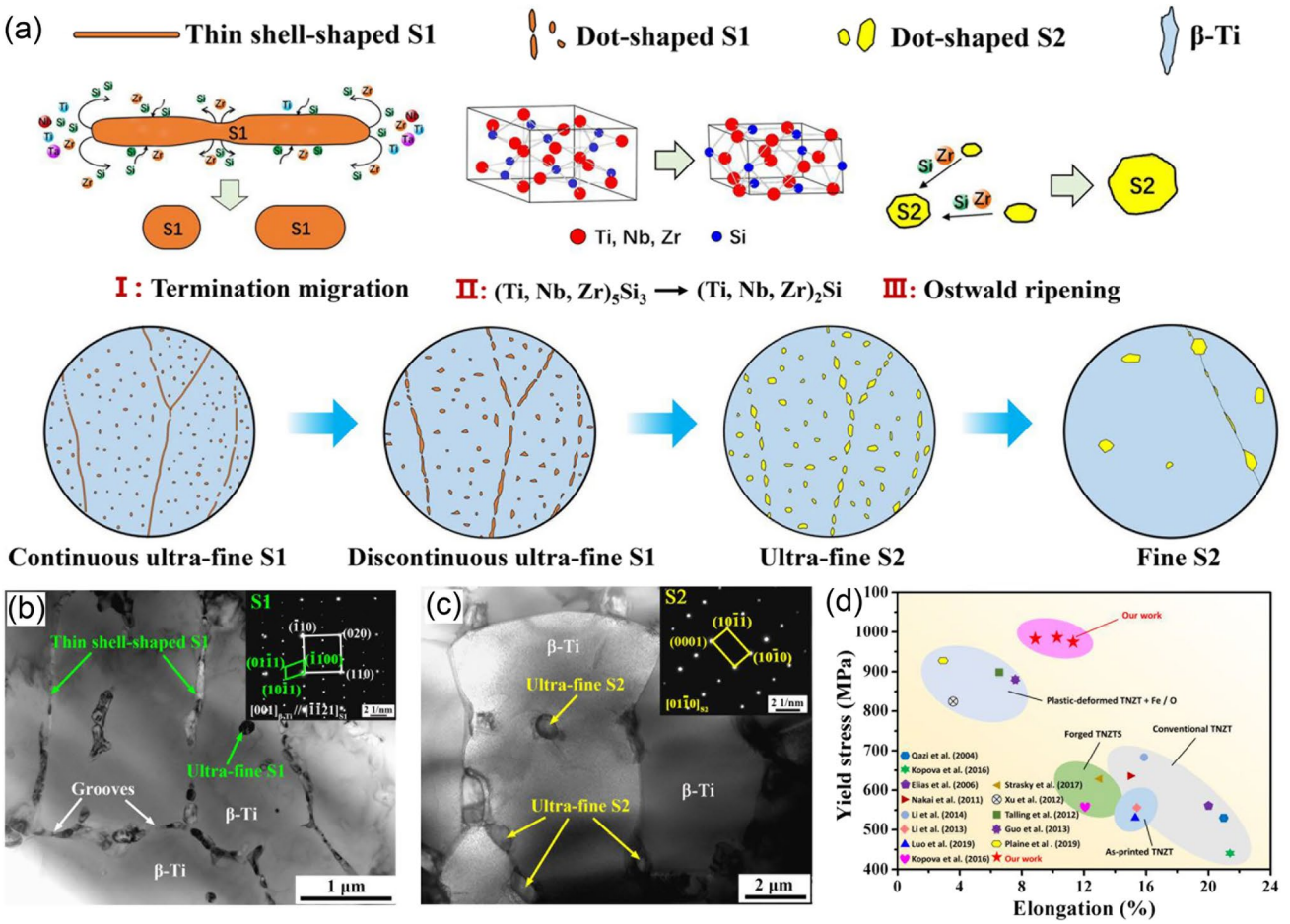

Fig. 4 **a** Schematic diagram of microstructure evolution and globularization mechanism with different heat treatment times, TEM morphology of the LPBF-ed **b** and heat-treated **c** Ti–Nb–Zr–Ta–Si alloys, **d** yield strength and elongation to failure of Ti–Nb–Zr–Ta alloys and Ti–Nb–Zr–Ta–Si alloys [65]

stable phase and finally achieving the alloy strengthening and toughening [65]. In conclusion, taking full advantage of the capabilities offered by AM for simultaneous and synergistic advancement of both alloy and process together can unlock the full potential of alloy performance.

4 Modulus Reduction of LPBF Biomedical β-Type Titanium Alloy

The elastic modulus of medical implant materials is an important mechanical property index to evaluate whether it is suitable for long-term implantation. The currently widely used Ti–6Al–4V alloy causes "stress shielding" due to its high elastic modulus (110 GPa) [66]. At present, there are three methods to reduce the elastic modulus of alloys: alloy design, lattice structure, and texture control. For alloy design, commonly used alloy design methods include molybdenum equivalent (Mo_{eq}) [67], average electron-to-atom ratio (e/a) [68, 69], d-electron method ($\overline{Bo}$–$\overline{Md}$ diagram) [18, 70, 71], and semiempirical approach [19]. The designed alloys include Ti–29Nb–13Ta–4.6Zr [72], Ti–29Nb–13Ta–4Mo [71], Ti–6Mo–4Zr [19], Ti–11Nb–38Zr [73], Ti–36Nb–2Ta–3Zr–0.3O [74], Ti–24Nb–4Zr–8Sn [75], etc. The elastic modulus of most β-type titanium alloys mentioned above is generally 40–80 GPa. It can be seen that the minimum limit elastic modulus of β-type titanium alloy designed by the composition design method is not less than 40 GPa, and there is a certain gap with the elastic modulus of human bone. Different from the alloy design, additively manufactured lattice structures of titanium alloys are another strategy to reduce the elastic modulus [21]. For example, Jam produced regular cubic cells by LPBF and low elastic modulus of 1 GPa was obtained along the cube side direction [76]. Besides, some other strategies, like addition of composites or alloying element or forming α nanoprecipitates to reduce modulus in heat-treated fabricated beta-Ti alloy, were also reported [77–79]. Texture control is another very effective strategy for preparing alloys with low elastic modulus. The following mainly introduces the research work on the LPBF to achieve low elastic modulus. Since LPBF has the characteristics of rapid solidification in micro-areas and fast cooling rate, the prepared alloy often has a 〈001〉 preferred orientation parallel to the building direction [80–83]. The 〈001〉 orientation is the direction with the lowest elastic modulus in cubic alloys, so it is commonly used to prepare 〈001〉 preferred orientation to control the elastic modulus. For example, Takayoshi obtained {001}⟨100⟩ cubic textures in different directions through unidirectional and 90° scanning strategies to achieve low elastic modulus [84]. Figure 5a, c shows the crystallographic textures in the three orthogonal cross-sections in samples fabricated by scan strategies *X* and *XY*, respectively. The corresponding {001} and {011} pole figures measured in the *y*–*z* plane are shown in Fig. 5b, d. When scan strategy *X* was applied, strong 〈001〉 and 〈011〉 alignments occurred along the scanning (*x*) and building (*z*) directions, respectively. On the contrary, scan strategy *XY* gave rise to a strong 〈001〉 alignments along the *x*, *y*, and *z* directions. As a result, causing the crystallographic orientation parallel to the building direction to change from 〈110〉 is 〈001〉, the elastic modulus decreases from 99.6 to 75.7 GPa. Different from changing the laser scanning strategy, when preparing Ti–Cr alloy by LPBF, changing the

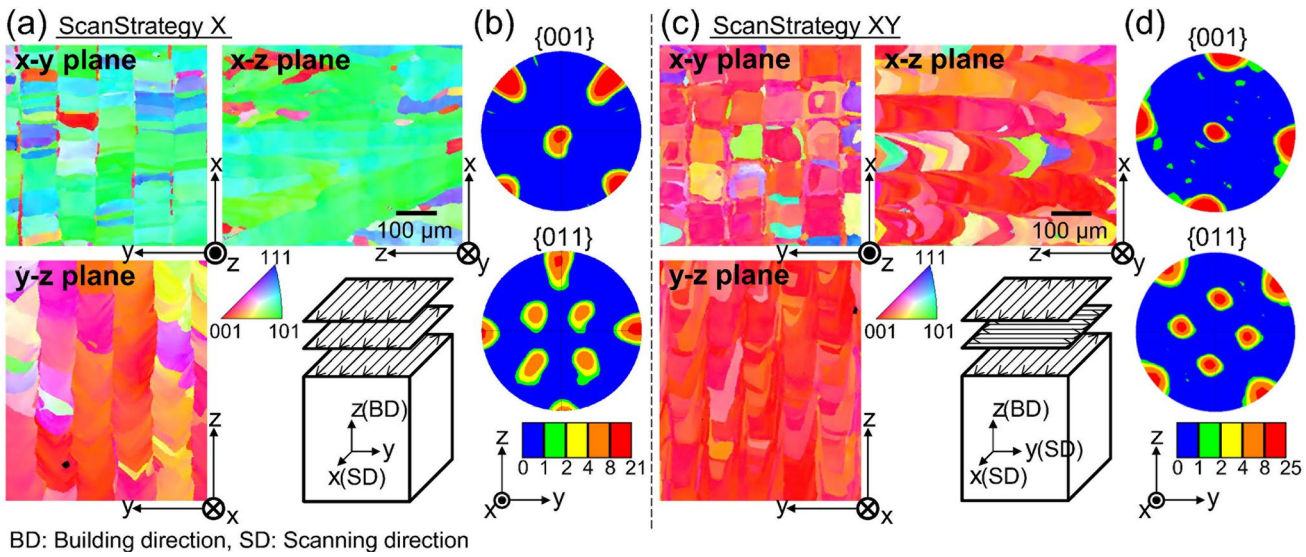

Fig. 5 **a**, **c** Inverse pole figure (IPF) images taken in the three orthogonal planes. **b**, **d** {001} and {011} pole figures of the products measured in the *y*–*z* plane [84]

laser energy density can also obtain the 〈001〉 orientation paralleled to the building direction [85]. Coincidentally, Chen et al. found that the 〈001〉 preferred orientation can be controlled by changing the laser scanning spacing in the LPBF-ed Ti–37Nb–6Sn alloy [86]. Combining with the in situ heat treatment of LPBF to precipitate the α″ phase, the Ti–37Nb–6Sn alloy has a low elastic modulus (66 GPa) and high tensile strength (891 MPa). Similar research on obtaining the 〈001〉 preferred orientation parallel to the building direction by changing the scanning spacing has also been reported in Inconel 718 [87] and NiTi alloy [88]. In summary, by changing some LPBF parameters, such as laser power, scanning speed, scanning spacing, and scanning strategy, 〈001〉 orientation parallel to the building direction can be achieved.

However, it is a challenge to achieve 〈001〉 orientation along arbitrary three-dimensional direction to meet the requirements of precise and controllable low elastic modulus that adapts to the complex stress environment of the human body. Then a question arises from this, what is the nature of controlling preferred 〈001〉 orientation, and how to achieve accurate and controllable low elastic modulus? As we all know, LPBF can be regarded as micro-area rapid solidification. Therefore, the extremely large temperature gradient (G) inside the melt pool and the solidification rate (R) at the front edge of the solid–liquid interface determine the solidification mode of the liquid metal [89–91]. For most β-type Ti alloys contain growth restriction elements such as Nb and Zr [90], the large temperature gradient of LPBF can easily cause large G/R. Therefore, most β-type Ti alloys solidify and grow in the form of columnar crystals. In this case, the 〈001〉 preferred growth direction of columnar crystals is controlled by the temperature gradient direction determined by the curvature of the melt pool interface [92]. The temperature gradient direction is generally perpendicular to the solid–liquid interface of the melt pool. Therefore, all factors that affect the geometry of the melt pool will affect the growth direction of columnar crystals (〈001〉 crystallographic orientation). Generally, the temperature gradient direction at the bottom of the melt pool is generally parallel to the building direction [93–95]. With the assistance of epitaxial growth, the alloy prepared by LPBF easily forms a 〈001〉 crystallographic orientation parallel to the building direction. But at the broadside of the melt pool, the temperature gradient direction of the melt pool boundary is not parallel to the building direction. So there is orientation selection under the competition between the columnar growth direction and the temperature gradient direction. If the temperature gradient direction of the melt pool boundary can be controlled, then the 〈001〉 crystallographic orientation can be customized, and ultimately the control of arbitrary 〈001〉 crystallographic orientation within the spatial range can be achieved. A new methodology for tailoring crystallographic orientation was established by fully considering the relationship between the melt pool geometry, temperature gradient, and the growth direction of columnar crystals, called multi-track coupled directional solidification (MTCDS) [96], as shown in Fig. 6. Figure 6a presents directional solidification along a specific growth direction of the columnar grain (GDCG) by precisely coupling multi-track melt pools. The CD sector has an almost unchanged temperature gradient direction (TGD), ensuring constant growth direction of the columnar grains. Figure 6b, c shows the scanning electron microscopy (SEM) and electron backscatter diffraction (EBSD) images of the single track. The transverse cross-section of the single track has a specific domain that consists of multiple columnar grains growing epitaxially from preexisting polycrystals. By precisely coupling multi-track melt pools with a tailored temperature gradient direction, 〈001〉 crystallographic orientation along specific spatial direction and corresponding low elastic modulus can be achieved (Fig. 6d–l). In addition, the letters S, C, U, and T with different 〈001〉 crystallographic orientation can be produced by MTCDS (Fig. 6m). This means that the MTCDS methodology can be generalized to a wide range of applications where specific crystallographic orientation at defined locations/region of a component is needed, especially for medical load-bearing bone implants with microstructure-controlled and locally variable elastic modulus for optimal stress shielding reduction. In summary, taking full account of the relationship among melt pool geometry, temperature gradient and columnar crystal growth direction during LPBF, it is expected that programming crystallographic orientation in additive-manufactured alloy to obtain the desired performance.

5 Corrosion Resistance and Biocompatibility of SLM Medical β Titanium Alloy

5.1 Corrosion Resistance

The complex fluid environment in the human body (Na^+, Cl^-, pH, and oxygen concentration) determines that the implant material must have good corrosion resistance to guarantee long service [5]. For most β-type Ti alloys including Nb and Ta, the formed stable Nb_2O_5, Ta_2O_5, and NbO_2 oxides can protect the alloy well and prevent further corrosion. Compared with the influence of alloying elements, the effect of microstructure on corrosion resistance is more important. Studies have shown that refining grain can reduce the passivation film with defects on the surface of titanium alloys, and improve the repair ability of passivation film [10, 97]. In addition, alloys with nanoscale grains are more likely to promote the formation of passivation films with better protection such as

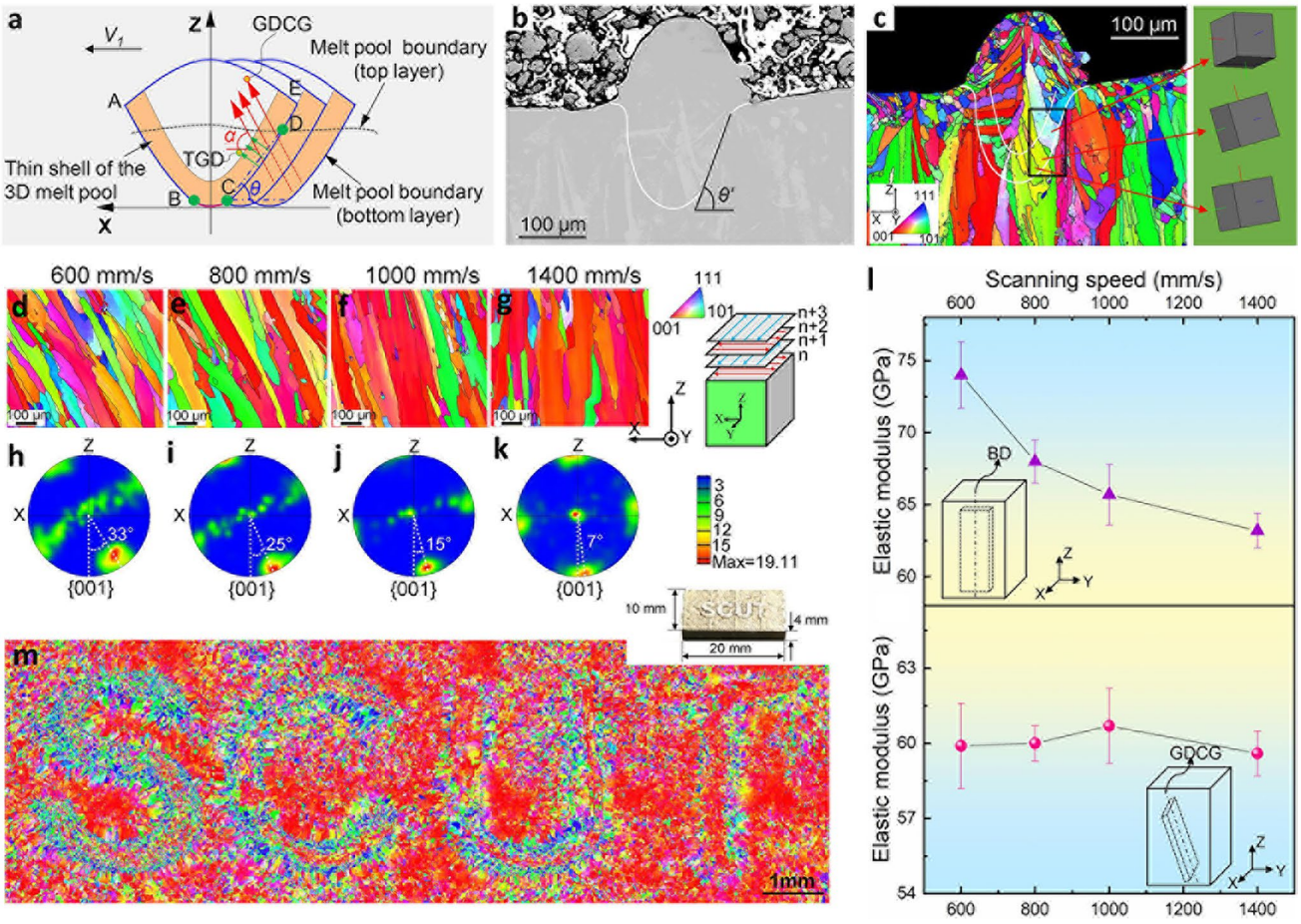

Fig. 6 **a** Schematic of MTCDS technique. Points B and E are the intersections between the top and bottom layers. Points B and C are the intersections between the left and right adjacent melt pools. The melt pool angle θ is the angle between line CD and the horizontal direction. The columnar grain angle α is the angle between the GDCG and the horizontal direction. The TGD is normal to the melt pool boundary and approximately normal to line CD. **b**, **c** SEM and EBSD images of single melt track. **d**–**g** Inverse pole figure and **h**–**k** 〈001〉 pole figure of 〈001〉 dendrites with different spatial orientation. **l** The elastic modulus along the construction direction with the 〈001〉 crystallographic orientation. **m** Letters S, C, U, and T produced by scanning speeds of 600, 800, 1000, and 1400 mm/s, respectively, exhibiting different deviation angles relative to the building direction. The surrounding matrix is produced at the scanning speed of 1400 mm/s [96]

Ti–25Nb–3Mo–3Zr–2Sn alloy [98]. This is due to the large number of grain boundaries that weaken the tendency of uneven distribution of alloy elements. Compared with β-type Ti alloys produced by traditional manufacturing methods, the LPBF-ed Ti alloys have smaller grain size, greater internal stress, and stronger texture distribution, so their corrosion resistance is different from that prepared by traditional manufacturing methods. For example, Ummethala et al. found that the LPBF-ed Ti–35Nb–7Zr–5Ta alloy has the highest polarization resistance and the lowest corrosion current in the direction of 45° from the building direction, which is due to the smaller grain size in the direction of 45°, the higher degree of lattice distortion, and the 〈110〉 preferred orientation [99]. In addition to the influence of the microstructure, the corrosion is related to the concentration and state of the solution. For example, compared with the oxide film formed in the dynamic condition, a slightly higher thickness and better corrosion resistance of the formed oxide film is formed in the static condition. The oxide film formed under the static condition has also better quality than the one formed under the dynamic condition, as shown in Fig. 7 [100]. Specifically, samples in static condition has a slightly lower passive current density than of in dynamic condition [101]. Besides, Qin et al. compared the corrosion behavior of printed and forged Ti–24Nb–4Zr–8Sn alloy in NaCl solution and Hank's solution, and the results showed that the polarization resistance and corrosion potential of the two alloys were basically similar, which they believed was caused by the single β phase of the two alloys rather than the technological difference [100]. It can be seen that the microstructure, phase composition, and grain size of β-type Ti alloys prepared by LPBF are important factors affecting their corrosion properties.

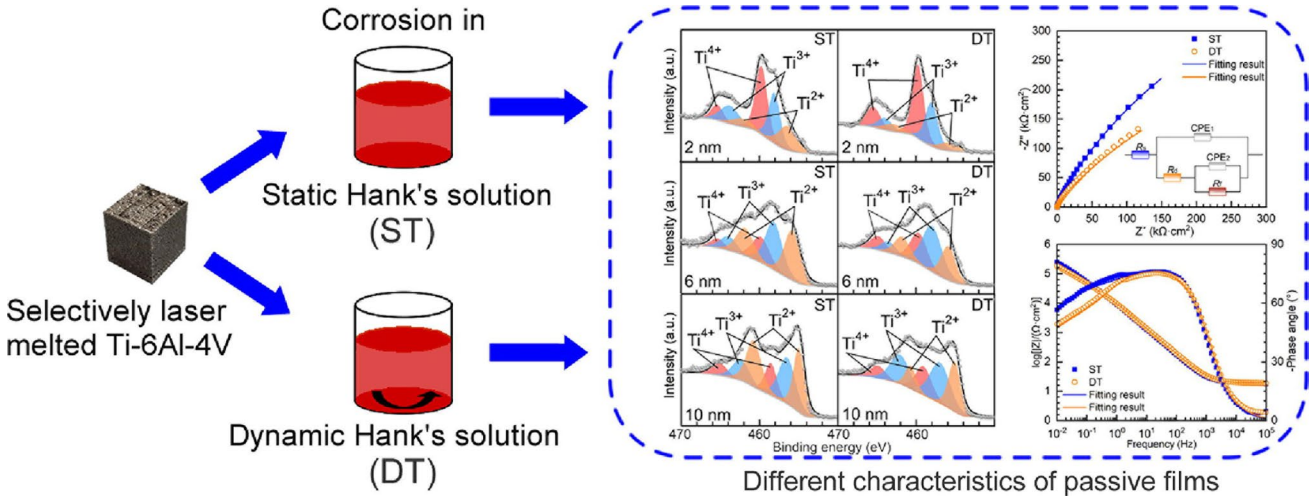

Fig. 7 Corrosion behavior and characteristics of passive films of laser powder bed fusion produced Ti–6Al–4V in static and dynamic Hank's solution [100]

5.2 Biocompatibility

According to the ISO interpretation, biocompatibility is the compatibility between a substance and a tissue or organ without rejection, which requires that the reaction between the implant and the host (blood response, immune response, tissue response, etc.) is moderate. Therefore, implant materials are first required that it does not contain toxic elements and will not cause any inflammation or allergic reaction in the human body after implantation [102]. For most of the medical β-type Ti alloys, it mainly contains Nb, Zr, Ta, Sn, and other bioactive elements, thereby good biocompatibility [103]. At present, the biocompatibility studies of LPBF-ed β-type Ti alloys are mainly divided into two categories: The first is to study the biocompatibility of the compositions inside the additive-manufactured alloys, that is, the use of mechanical processing to remove the surface printing layer, and the biological characteristics of the implant material such as cytotoxicity, cell proliferation, cell paste, and genetic toxicity are characterized by in vitro cell experiments and animal experiments. For example, Luo et al. [104] found through in vitro cell experiments that LPBF-ed Ti–30Nb–5Ta–3Zr alloy had better cell proliferation ability than Ti–6Al–4V alloy. Similarly, other LPBF-ed β-type titanium alloys, such as Ti–25Nb [105], Ti–34Nb–13Ta–5Zr [106], and Ti–15Ta–10.5Zr [107], all show good biocompatibility. The second category is to study the biocompatibility of LPBF-ed porous β-type titanium alloys. The surface of the alloy was not machined, or only a simple treatment was carried out to remove the excess powder on the surface when conducting measurements. For example, Guo conducted in vitro osteogenesis and in vivo bone integration experiments of Ti–36Nb–2Zr–2Ta porous structure on human bone marrow mesenchymal stem cells and rabbit lateral femoral condyle, respectively [108]. They found that Ti–36Nb–2Zr–2Ta porous structure promoted bone regeneration and bone integration more effectively than Ti–6Al–4V. It is not difficult to see that the β-type titanium alloys have good biocompatibility, which is due to the inclusion of bioactive elements Nb, Zr, Ta, and so on. In addition, Sun et al. found in animal experiments that the introduction of Si into Ti–Nb–Zr–Ta alloy was conducive to enhancing cell adhesion, proliferation and differentiation, and accelerated bone formation [109]. In view of the effect of Si element on mechanical properties and biocompatibility of alloys, it is reported that the introduction of Si can refine grain, strengthen mechanical properties, and improve biocompatibility in LPBF-ed Ti–Nb–Zr–Ta–Si alloys [7]. Therefore, it can be seen that Si as a bioactive element is beneficial to improve the biocompatibility of the alloy.

6 Conclusions and Prospects

Although LPBF has great advantages and a series of progress in the manufacture of orthopedic implant β-type Ti alloys, there are still big challenges to be widely used in clinical medicine like Ti-6AL-4V, mainly the following points:

1. Extreme high temperature gradients and rapid solidification rates lead to uncontrollable non-equilibrium phases and microstructure. Various metallurgical processes make it difficult to control and predict the stability and heat transfer of melt pools. This often causes certain problems, such as layer separation, residual stress leading to warping and balling effect. Although the above

problems can be avoided through the optimization of process parameters, the LPBF dynamic manufacturing process significantly affects the stability of the forming quality and the homogenization of the microstructure. In particular, pores can be largely eliminated by parameter optimization, but they are inevitably mixed with pores due to powder splashing and denudation. These are difficult to ensure the reliability and stability of parts in service.

2. At present, there are many kinds of LPBF-ed β-type Ti alloys, most of the research focuses on how to improve the strength and reduce the elastic modulus. Research on biocompatibility is still in the experimental stage. In order to ensure the long-term effective service of orthopedic implants, it is important to improve their biocompatibility. Therefore, it is necessary to rapidly promote the various clinical medical verification and ethical review of LPBF-ed β-type Ti alloys, which is crucial to rapidly promote the clinical application of β-type Ti alloys for orthopedic implants.
3. The gas-atomized spherical metal powder used in LPBF is generally melted to prepare the bar, then the gas-atomized powder, and finally the metal powder suitable for LPBF. This makes metal powder expensive. In order to solve this problem, the range of powder products such as metals should be increased and improved, thereby reducing costs. For example, more affordable hydrogenated–dehydrogenerated and hydride–dehydride cp-Ti powders have been developed as alternatives to gas-atomized spherical powders to produce bone implants via LPBF. The outcomes of both showed improved mechanical strength and biocompatibility. Another reason for the high cost of LPBF is that the performance of the powder will be greatly deteriorated after repeated use, so that new powder has to be used to ensure the performance of the component. A discharge plasma modification (DPM) method to heal out-of-specification Ti powder recycled during LPBF has been proposed, which can be used to manufacture high-performance bulk Ti via LPBF [110]. This provides a new inspiration for powder reuse. In addition to considering the cost of the powder, the effect of the powder produced by hydride–dehydride technique on the required properties also needs to be considered. For example, the thermal oxidation could improve the wear and fatigue properties of TNT5Zr–0.2O alloys manufactured by LPBF [111]. Therefore, there are still challenges in balancing the cost of the powder with the performance of the component.

Acknowledgements This work was supported financially by the National Natural Science Foundation of China (Nos. 52304397 and U19A2085), the Guangdong Basic and Applied Basic Research Foundation (Nos. 2022B1515120082 and 2019B030302010), the Guangdong Science and Technology Innovation Project (No. 2021TX06C111), and the Optical Valley Science Research Project, WEHDZ (No. 2019001).

Declarations

Conflict of interest The authors state that there are no conflicts of interest to disclose.

References

[1] L.C. Zhang, L.Y. Chen, Adv. Eng. Mater. **21**, 1801215 (2019)
[2] H.E. Lange, D. Hohlfeld, R. Bader, D. Kluess, Smart Mater. Struct. **29**, 115051 (2020)
[3] Y. Li, C. Yang, H. Zhao, S. Qu, X. Li, Y. Li, Materials **73**, 1709 (2014)
[4] N. Dai, L.C. Zhang, J. Zhang, Q. Chen, M. Wu, Corros. Sci. **102**, 484 (2016)
[5] Q. Chen, G.A. Thouas, Mater. Sci. Eng. R **87**, 1 (2015)
[6] S.F. Jawed, C.D. Rabadia, Y.J. Liu, L.Q. Wang, P. Qin, Y.H. Li, X.H. Zhang, L.C. Zhang, Mater. Sci. Eng. C **110**, 110728 (2020)
[7] X. Luo, C. Yang, R.Y. Li, H. Wang, H.Z. Lu, T. Song, H.W. Ma, D.D. Li, A. Gebert, Y.Y. Li, Biomater. Adv. **133**, 112625 (2022)
[8] X. Luo, T. Song, F. Wang, H. Lu, L. Kang, H. Ma, D. Li, A. Gebert, C. Yang, Adv. Powder Mater. **2**, 100118 (2023)
[9] S. Bose, D. Ke, H. Sahasrabudhe, A. Bandyopadhyay, Prog. Mater. Sci. **93**, 45 (2018)
[10] N. Hu, L. Xie, Q. Liao, A. Gao, Y. Zheng, H. Pan, L. Tong, D. Yang, N. Gao, M.J. Starink, P.K. Chu, H. Wang, Acta Biomater. **126**, 524 (2021)
[11] L. Zhou, T. Yuan, R. Li, J. Tang, M. Wang, F. Mei, J. Alloys Compd. **762**, 289 (2018)
[12] X.M. Ma, W. Sun, J. Alloys Compd. **509**, 294 (2011)
[13] N. Hafeez, S. Liu, E. Lu, L. Wang, R. Liu, W. Lu, L.C. Zhang, J. Alloys Compd. **790**, 117 (2019)
[14] L.C. Zhang, D. Klemm, J. Eckert, Y.L. Hao, T.B. Sercombe, Scr. Mater. **65**, 21 (2011)
[15] Y.J. Liu, S.J. Li, H.L. Wang, W.T. Hou, Y.L. Hao, R. Yang, T.B. Sercombe, L.C. Zhang, Acta Mater. **113**, 56 (2016)
[16] J. Chen, X. Liao, J. Shu, L. Zhou, C. Li, Y. Ren, Y. Niu, Mater. Sci. Eng. A **826**, 141962 (2021)
[17] D. Zhao, C. Han, Y. Li, J. Li, K. Zhou, Q. Wei, J. Liu, Y. Shi, J. Alloys Compd. **804**, 288 (2019)
[18] Y.H. Li, C. Yang, F. Wang, H.D. Zhao, S.G. Qu, X.Q. Li, W.W. Zhang, Y.Y. Li, Mater. Des. **85**, 7 (2015)
[19] C.H. Wang, A.M. Russell, G.H. Cao, Scr. Mater. **158**, 62 (2019)
[20] H.Z. Lu, C. Yang, X. Luo, H.W. Ma, B. Song, Y.Y. Li, L.C. Zhang, Mater. Sci. Eng. A **763**, 138166 (2019)
[21] L.Y. Chen, S.X. Liang, Y. Liu, L.C. Zhang, Mater. Sci. Eng. R **146**, 100648 (2021)
[22] D. Gu, X. Shi, R. Poprawe, D.L. Bourell, R. Setchi, J. Zhu, Science **372**, 1487 (2021)
[23] Y.L. Wang, K.C. Chan, Mater. Sci. Eng. A **876**, 145164 (2023)
[24] Y. Zhang, S. Ye, H. Ke, K.C. Chan, W. Wang, Mater. Des. **229**, 111891 (2023)
[25] Y. Zhang, B. Qin, K. Chan, R. Lupoi, S. Yin, Y. Xie, S. Ye, P. Yu, H. Ke, W. Wang, J. Manuf. Process. **94**, 413 (2023)
[26] L.C. Zhang, H. Attar, Adv. Eng. Mater. **18**, 463 (2016)
[27] L. Liu, Q. Ding, Y. Zhong, J. Zou, J. Wu, Y.L. Chiu, J. Li, Z. Zhang, Q. Yu, Z. Shen, Mater. Today **21**, 354 (2018)
[28] X. Luo, D.D. Li, C. Yang, A. Gebert, H.Z. Lu, T. Song, H.W. Ma, L.M. Kang, Y. Long, Y.Y. Li, Addit. Manuf. **51**, 102640 (2022)

[29] Y.M. Wang, T. Voisin, J.T. McKeown, J. Ye, N.P. Calta, Z. Li, Z. Zeng, Y. Zhang, W. Chen, T.T. Roehling, R.T. Ott, M.K. Santala, P.J. Depond, M.J. Matthews, A.V. Hamza, T. Zhu, Nat. Mater. **17**, 63 (2018)
[30] X. Luo, C. Yang, Z.Q. Fu, L.H. Liu, H.Z. Lu, H.W. Ma, Z. Wang, D.D. Li, L.C. Zhang, Y.Y. Li, Mater. Sci. Eng. A **823**, 141731 (2021)
[31] Y. Huang, C. Shen, X. Ji, F. Li, Y. Zhang, X. Hua, J. Mater. Process. Technol. **283**, 116721 (2020)
[32] R. Cunningham, C. Zhao, N. Parab, C. Kantzos, J. Pauza, K. Fezzaa, T. Sun, A.D. Rollett, Science **363**, 849 (2019)
[33] H.Z. Lu, L.H. Liu, C. Yang, X. Luo, C.H. Song, Z. Wang, J. Wang, Y.D. Su, Y.F. Ding, L.C. Zhang, Y.Y. Li, J. Mater. Sci. Technol. **101**, 205 (2022)
[34] H.Z. Lu, H.W. Ma, W.S. Cai, X. Luo, Z. Wang, C.H. Song, S. Yin, C. Yang, Acta Mater. **219**, 117261 (2021)
[35] D. Zhang, D. Qiu, M.A. Gibson, Y. Zheng, H.L. Fraser, D.H. StJohn, M.A. Easton, Nature **576**, 91 (2019)
[36] J.H. Martin, B.D. Yahata, J.M. Hundley, J.A. Mayer, T.A. Schaedler, T.M. Pollock, Nature **549**, 365 (2017)
[37] T.L. Zhang, Z.H. Huang, T. Yang, H.J. Kong, J.H. Luan, A.D. Wang, D. Wang, W. Kuo, Y.Z. Wang, C.T. Liu, Science **374**, 478 (2021)
[38] D. Ouyang, P. Zhang, C. Zhang, N. Li, K.C. Chan, L. Liu, Mater. Sci. Eng. A **867**, 144745 (2023)
[39] H.Z. Lu, H.W. Ma, W.S. Cai, X. Luo, S.G. Qu, J. Wang, R. Lupoi, S. Yin, C. Yang, J. Mater. Process. Technol. **303**, 117546 (2022)
[40] H.Z. Lu, L.H. Liu, X. Luo, H.W. Ma, W.S. Cai, R. Lupoi, S. Yin, C. Yang, Mater. Des. **232**, 112107 (2023)
[41] L.C. Zhang, L.Y. Chen, S. Zhou, Z. Luo, J. Alloys Compd. **936**, 168099 (2023)
[42] P. Kurnsteiner, M.B. Wilms, A. Weisheit, B. Gault, E.A. Jagle, D. Raabe, Nature **582**, 515 (2020)
[43] H.Z. Lu, T. Chen, L.H. Liu, H. Wang, X. Luo, C.H. Song, Z. Wang, C. Yang, Virtual Phys. Prototyp. **17**, 563 (2022)
[44] T. DebRoy, H.L. Wei, J.S. Zuback, T. Mukherjee, J.W. Elmer, J.O. Milewski, A.M. Beese, A. Wilson-Heid, A. De, W. Zhang, Prog. Mater. Sci. **92**, 112 (2018)
[45] P.S. Cook, A.B. Murphy, Addit. Manuf. **31**, 100909 (2020)
[46] J.H. Tan, W.L.E. Wong, K.W. Dalgarno, Addit. Manuf. **18**, 228 (2017)
[47] D.D. Gu, W. Meiners, K. Wissenbach, R. Poprawe, Int. Mater. Rev. **57**, 133 (2013)
[48] T. Scharowsky, F. Osmanlic, R.F. Singer, C. Körner, Appl. Phys. A **114**, 1303 (2014)
[49] N.K. Tolochko, S.E. Mozzharov, I.A. Yadroitsev, T. Laoui, L. Froyen, V.I. Titov, M.B. Ignatiev, Rapid Prototyp. J. **10**, 78 (2004)
[50] I. Yadroitsev, P. Bertrand, I. Smurov, Appl. Surf. Sci. **253**, 8064 (2007)
[51] I. Yadroitsev, A. Gusarov, I. Yadroitsava, I. Smurov, J. Mater. Process. Technol. **210**, 1624 (2010)
[52] J. Wang, R. Zhu, Y. Liu, L. Zhang, Adv. Powder Mater. **2**, 100137 (2023)
[53] J.P. Kruth, G. Levy, F. Klocke, T. Childs, C.I.R.P. Ann, Manuf. Technol. **56**, 730 (2007)
[54] E. Louvis, P. Fox, C.J. Sutcliffe, J. Mater. Process. Technol. **211**, 275 (2011)
[55] M.J. Matthews, G. Guss, S.A. Khairallah, A.M. Rubenchik, P.J. Depond, W.E. King, Acta Mater. **114**, 33 (2016)
[56] S. Das, Adv. Eng. Mater. **5**, 701 (2010)
[57] P. Mercelis, J. Kruth, Rapid Prototyp. J. **12**, 254 (2006)
[58] M.F. Zaeh, G. Branner, Prod. Eng. **4**, 35 (2010)
[59] Y.J. Liu, Y.S. Zhang, L.C. Zhang, Materialia **6**, 100299 (2019)
[60] R. Ummethala, P.S. Karamched, S. Rathinavelu, N. Singh, A. Aggarwal, K. Sun, E. Ivanov, L. Kollo, I. Okulov, J. Eckert, K.G. Prashanth, Materialia **14**, 100941 (2020)
[61] R. Duan, S. Li, B. Cai, W. Zhu, F. Ren, M.M. Attallah, Addit. Manuf. **37**, 101708 (2021)
[62] L. Zhou, T. Yuan, R. Li, J. Tang, M. Wang, L. Li, C. Chen, J. Alloys Compd. **775**, 1164 (2019)
[63] C.L. Yang, Z.J. Zhang, S.J. Li, Y.J. Liu, T.B. Sercombe, W.T. Hou, P. Zhang, Y.K. Zhu, Y.L. Hao, Z.F. Zhang, R. Yang, Mater. Des. **157**, 52 (2018)
[64] G.H. Zhao, X. Xu, D. Dye, P.E.J. Rivera-Diaz-del-Castillo, Acta Mater. **183**, 155 (2020)
[65] X. Luo, L.H. Liu, C. Yang, H.Z. Lu, H.W. Ma, Z. Wang, D.D. Li, L.C. Zhang, Y.Y. Li, J. Mater. Sci. Technol. **68**, 112 (2021)
[66] M. Niinomi, J. Mech. Behav. Biomed. Mater. **1**, 30 (2008)
[67] S. Ehtemam-Haghighi, Y. Liu, G. Cao, L.C. Zhang, Mater. Sci. Eng. C **60**, 503 (2016)
[68] Y.L. Hao, S.J. Li, S.Y. Sun, C.Y. Zheng, R. Yang, Acta Biomater. **3**, 277 (2007)
[69] P. Laheurte, F. Prima, A. Eberhardt, T. Gloriant, M. Wary, E. Patoor, J. Mech. Behav. Biomed. Mater. **3**, 565 (2010)
[70] M. Abdel-Hady, K. Hinoshita, M. Morinaga, Scr. Mater. **55**, 477 (2006)
[71] D. Kuroda, M. Niinomi, M. Morinaga, Y. Kato, T. Yashiro, Mater. Sci. Eng. A **243**, 244 (1998)
[72] M. Morinaga, N. Yukawa, T. Maya, K. Sone, H. Adachi, in *Sixth World Conference on Titanium*. III, 6–9 June 1988, pp. 1601-1606
[73] L. You, X. Song, Scr. Mater. **67**, 57 (2012)
[74] T. Saito, T. Furuta, J.H. Hwang, S. Kuramoto, K. Nishino, N. Suzuki, R. Chen, A. Yamada, K. Ito, Y. Seno, T. Nonaka, H. Ikehata, N. Nagasako, C. Iwamoto, Y. Ikuhara, T. Sakuma, Science **300**, 464 (2003)
[75] Y.L. Hao, S.J. Li, B.B. Sun, M.L. Sui, R. Yang, Phys. Rev. Lett. **98**, 216405 (2007)
[76] A. Jam, A. du Plessis, C. Lora, S. Raghavendra, M. Pellizzari, M. Benedetti, Addit. Manuf. **50**, 102556 (2022)
[77] M.M. Zhou, P. Wang, L. Xu, L. Deng, J.F. Qi, L.C. Zhang, J. Alloys Compd. **960**, 170512 (2023)
[78] H. Schaal, P. Castany, P. Laheurte, T. Gloriant, J. Alloys Compd. **96**, 6171539 (2023)
[79] Q. Shi, S. Yang, Y. Sun, B.V. Meerbeek, C. Politis, Mater. Sci. Eng. A **857**, 144101 (2022)
[80] S. Paul, J. Liu, S.T. Strayer, Y. Zhao, S. Sridar, M.A. Klecka, W. Xiong, A.C. To, Addit. Manuf. **36**, 101611 (2020)
[81] S. Pilz, T. Gustmann, F. Günther, M. Zimmermann, U. Kühn, A. Gebert, Mater. Des. **216**, 110516 (2022)
[82] K. Hagihara, T. Nakano, JOM **74**, 1760 (2021)
[83] S.H. Sun, K. Hagihara, T. Ishimoto, R. Suganuma, Y.F. Xue, T. Nakano, Addit. Manuf. **47**, 102329 (2021)
[84] T. Ishimoto, K. Hagihara, K. Hisamoto, S.H. Sun, T. Nakano, Scr. Mater. **132**, 34 (2017)
[85] T. Nagase, T. Hori, M. Todai, S.-H. Sun, T. Nakano, Mater. Des. **173**, 107771 (2019)
[86] W. Chen, C. Chen, X. Zi, X. Cheng, X. Zhang, Y.C. Lin, K. Zhou, Mater. Sci. Eng. A **726**, 240 (2018)
[87] N. Nadammal, S. Cabeza, T. Mishurova, T. Thiede, A. Kromm, C. Seyfert, L. Farahbod, C. Haberland, J.A. Schneider, P.D. Portella, G. Bruno, Mater. Des. **134**, 139 (2017)
[88] N.S. Moghaddam, S. Saedi, A. Amerinatanzi, A. Hinojos, A. Ramazani, J. Kundin, M.J. Mills, H. Karaca, M. Elahinia, Sci. Rep. **9**, 41 (2019)
[89] A. Hadadzadeh, B.S. Amirkhiz, J. Li, M. Mohammadi, Addit. Manuf. **23**, 121 (2018)
[90] M.J. Bermingham, D.H. StJohn, J. Krynen, S. Tedman-Jones, M.S. Dargusch, Acta Mater. **168**, 261 (2019)

[91] B. Vrancken, L. Thijs, J.P. Kruth, J. Van Humbeeck, Acta Mater. **68**, 150 (2014)
[92] S.E. Saghaian, M. Nematollahi, G. Toker, A. Hinojos, N. Shayesteh Moghaddam, S. Saedi, C.Y. Lu, M. Javad Mahtabi, M.J. Mills, M. Elahinia, H.E. Karaca, Opt. Laser Technol. **149**, 107680 (2022)
[93] J.G. Pauza, W.A. Tayon, A.D. Rollett, Modell. Simul. Mater. Sci. Eng. **29**, 055019 (2021)
[94] F. Xiong, C. Huang, O.L. Kafka, Y. Lian, W. Yan, M. Chen, D. Fang, Mater. Des. **199**, 109410 (2021)
[95] T. Ishimoto, S. Wu, Y. Ito, S.-H. Sun, H. Amano, T. Nakano, ISIJ Int. **60**, 1758 (2020)
[96] X. Luo, T. Song, A. Gebert, K. Neufeld, I. Kaban, H. Ma, W. Cai, H. Lu, D. Li, N. Li, Y. Li, C. Yang, Adv. Sci. **10**, 2302884 (2023)
[97] J. Li, S.J. Li, Y.L. Hao, H.H. Huang, Y. Bai, Y.Q. Hao, Z. Guo, J.Q. Xue, R. Yang, Acta Biomater. **10**, 2866 (2014)
[98] R. Huang, Y. Han, Mater. Sci. Eng. C **33**, 2353 (2013)
[99] R. Ummethala, J. Jayaraj, P.S. Karamched, S. Rathinavelu, N. Singh, K.B. Surreddi, K.G. Prashanth, J. Mater. Eng. Perform. **30**, 7967 (2021)
[100] P. Qin, Y. Chen, Y.J. Liu, J. Zhang, L.Y. Chen, Y. Li, X. Zhang, C. Cao, H. Sun, L.C. Zhang, A.C.S. Biomater, Sci. Eng. **5**, 1141 (2019)
[101] L.Y. Chen, H.Y. Zhang, C. Zheng, H.Y. Yang, P. Qin, C. Zhao, S. Lu, S.X. Liang, L. Chai, L.C. Zhang, Mater. Des. **208**, 109907 (2021)
[102] K. Prasad, O. Bazaka, M. Chua, M. Rochford, L. Fedrick, J. Spoor, R. Symes, M. Tieppo, C. Collins, A. Cao, D. Markwell, K.K. Ostrikov, K. Bazaka, Materials **10**, 884 (2017)
[103] M. Geetha, A.K. Singh, R. Asokamani, A.K. Gogia, Prog. Mater. Sci. **54**, 397 (2009)
[104] J.P. Luo, J.F. Sun, Y.J. Huang, J.H. Zhang, Y.D. Zhang, D.P. Zhao, M. Yan, Mater. Sci. Eng. C **97**, 275 (2019)
[105] D. Zhao, C. Han, J. Li, J. Liu, Q. Wei, Mater. Sci. Eng. C **111**, 110784 (2020)
[106] W. Kong, S.C. Cox, Y. Lu, V. Villapun, X. Xiao, W. Ma, M. Liu, M.M. Attallah, Mater. Sci. Eng. C **131**, 112486 (2021)
[107] L. Yan, Y. Yuan, L. Ouyang, H. Li, A. Mirzasadeghi, L. Li, J. Alloys Compd. **688**, 156 (2016)
[108] Y. Guo, J. Wu, K. Xie, J. Tan, Y. Yang, S. Zhao, L. Wang, W. Jiang, Y. Hao, A.C.S. Biomater, Sci. Eng. **5**, 6463 (2019)
[109] Y. Sun, Y. Song, J. Zuo, S. Wang, Z. Gao, RSC Adv. **5**, 101794 (2015)
[110] Z. Liu, T. Chen, W.S. Cai, H.Z. Lu, Z.C. Lu, D. Wang, X.Q. Li, X.Y. Zhang, C. Yang, Scr. Mater. **236**, 115662 (2023)
[111] W. Kong, V.M. Villapun, Y. Lu, L.N. Carter, M. Kuang, S. Cox, M.M. Attallah, J. Alloys Compd. **929**, 167264 (2022)